Noname manuscript No.
(will be inserted by the editor)

Geometric Steerable Medial Maps

Sergio Vera · Debora Gil · Agnés Borràs · Marius George Linguraru · Miguel Angel González

Accepted: february 2013. Final version featured in the Machine Vision and Applications Journal ISSN: 1432-1769 (electronic version)

Abstract In order to provide more intuitive and easily interpretable representations of complex shapes/organs, medial manifolds should reach a compromise between simplicity in geometry and capability for restoring the anatomy/shape of the organ/volume. Existing morphological methods show excellent results when applied to 2D objects, but their quality drops across dimensions.

This paper contributes to the computation of medial manifolds from a theoretical and a practical point of view. First, we introduce a continuous operator for accurate and efficient computation of medial structures of arbitrary dimension. Second, we present a validation protocol for assessing the suitability of medial surfaces for anatomical representation in medical applications. We evaluate quantitatively the performance of our method with respect to existing approaches and show its higher performance for medical imaging applications in terms of medial simplicity and capability of reconstructing the anatomical volume.

Keywords Medial Representations · Medial Manifolds · Comparison · Surface · Reconstruction

Sergio Vera, Miguel Angel González
Alma I.T. Systems, Barcelona, Spain
E-mail: sergio.vera@alma3d.com
E-mail: miguel.gonzalez@alma3d.com

Debora Gil, Agnés Borràs
Computer Vision Center, Universitat Autònoma de Barcelona, Spain
E-mail: agnesba@cvc.uab.es
E-mail: debora@cvc.uab.es

Marius George Linguraru
Sheikh Zayed Institute for Pediatric Surgical Innovation, Children's National Medical Center, Washington DC, USA

1 Introduction

Medial representations have gained increased popularity at describing [45,44, 46,47,40] and segmenting structures [48,21,10]. While other surface representation methods model only the external surface of objects, medial representations can model also the interior of the shape by providing a radial perpendicular coordinate that extends from the medial surface [6]. In medical applications, this is particularly useful for addressing the following topics:

- *Localization of injured tissue.* The radial coordinate of medial representations allows parameterizing [15,34] the (possibly diseased) parenchyma of organs, as well as their internal vascular system, powerful sources of information in organ functionality, analysis and diagnosis
- *Segmentation of medical images.* In medical imaging, techniques such as M-Reps [28,13] and CM-Reps [51,39] have shown the potential to describe complex shapes in a versatile manner. Using information of a medial surface for medical imaging segmentation has proven to improve segmentation results [29,37]. It follows that deformable medial modelling has been used in a variety of medical imaging analysis applications, including computational neuroanatomy [53,35], 3D cardiac modelling [36] or cancer treatment planning [33,11].
- *Modelization of anatomy.* In shape analysis, medial representations can provide better information than Point Distribution Models (PDM) since they can model not only the shape but also the interior variations [52]. Medial manifolds of organs have proved robust and accurate to study group differences in internal structures of the brain [35,34]. They also provide more intuitive and easily interpretable representations of complex organs [50] and their relative positions [25].

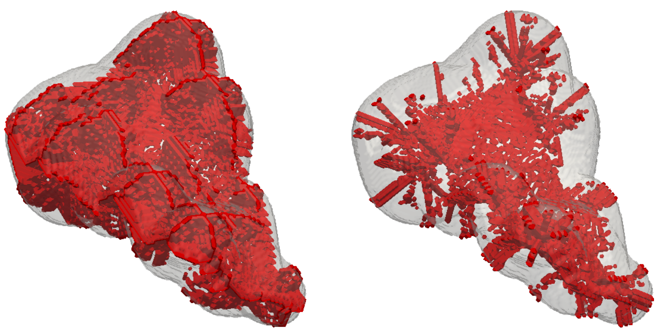

(a) (b)

Fig. 1: Medial surfaces obtained using a 6-connected neighborhood, (a), and a 26 connected neighborhood, (b).

In order to accurately address the above topics, the medial representation has to achieve a good reconstruction of the full anatomy and guarantee that the boundaries of the organ are reached from the medial surface. It follows that anatomical medial manifolds must be simple enough to allow an easy generation of the radial axis, but complete enough to allow a satisfactory reconstruction of the whole volume. Representations of the original anatomical geometry are accurate as far as the extracted medial manifold satisfies [30]:

- *Homotopy*: The medial manifold has to have the same topology (same number of foreground objects and holes) as the original shape .
- *Thinness*: The resulting medial shape should be one pixel wide. The specific connectivity used to consider two pixels as adjacent, should be considered at this point.
- *Medialness*: The medial structure should lie as close as possible to the center of the original object.

Many methods are based on morphological thinning of either a binary segmentation or, in order to ensure medialness, the distance map to the boundary [8,30,32,4,27,20,38]. Such methods require the topological definition of a neighborhood set and conditions for the removal of *simple voxels*, i.e. voxels that can be removed without changing the topology of the object. These topology definitions are trivial in 2D, but their complexity increases exponentially with the dimension of the embedding space [22]. Further, simplicity tests alone only produce (1D) medial axis so additional tests are needed to know if a voxel lies in a surface and thus cannot be deleted even if it is simple [30,20]. Finally, small changes in surface and simplicity tests or in the order in which voxels are traversed generate completely different surfaces (as illustrated in Fig. 1).

Surface tests might introduce medial axis segments in the medial surface, which is against the mathematical definition of manifold. Additionally, since medial axes hinder the calculation of the radial coordinate, such medial structures are ill-conditioned for the generation of proper medial representations [44]. Consequently, they may require further pruning before their use in subsequent applications [30,3,20]. However, there is no easy way to tell which manifolds can be safely removed without hurting the capability of representation of anatomical structures. Pruning strategies rely on additional topological tests for removal of unwanted medial axis [30,3] or surface segments [20]. However, an aggressive pruning might break topology or remove important medial manifold segments for shape reconstruction.

Another line of research approximates medial surfaces from a tetrahedral mesh of a set of points sampled on the object boundary [12,31,2,3]. These methods provide an elegant conceptual description but present some practical limitations. First, the density of the boundary sampling required for the right medial topology is a-priori unknown. This leads to a selective refinement of the initial sampling based on topological and geometric tests which complexity significantly increases for capturing anatomical finest details [12]. Second, in 3D it is not always guaranteed convergence to the medial surface [23], the approximation is prone to fail at branches [12,31] and might generate multiple spikes [3].

Energy-based methodologies [1,42,41] constitute a completely different approach since medial points are characterized as local maxima of a potential map. A main advantage over topological inspired methods is that the geometric properties of the medial surface are determined by the definition of the potential map. The shape representation introduced in [1] relies on a potential map that represents distances to the object boundary avoiding the generation of extra medial branches at boundary corners. Medial surfaces are reconstructed by tracking the gradient of the potential map from the object boundary points. This introduces two main limitations. On one hand, it is prone to give non-connected medial surfaces [1]. On the other hand, the step is so computationally expensive that it is hardly feasible over dimension two. In a previous work [41], we explored the potential of energy-based methods combined with a Non-Maxima Suppression (NMS) scheme for extracting medial surfaces. Experiments on a reduced set of synthetic shapes showed the capability of energy-based methods for surpassing the performance of thinning methodologies in terms of medialness (thanks to the energy based scheme) and thinness (thanks to NMS binarization). A main concern was a significant drop of the response at branches and the generation of internal holes in medial surfaces, which violated the homotopy condition. In [41], homotopy was partially recovered using morphological closing. Recently, we identified the theoretical weaknesses of existing ridge detectors in order to define a novel energy [42] able to produce medial surfaces achieving a compromise between simplicity and reconstruction power for representation and parametrization of anatomical structures [43].

In this work, we contribute to the computation of medial manifolds from a theoretical and practical point of view. From the theoretical side, we propose a two-step method that combines the best of [42] and [41] in order to get medial surfaces fulfilling the three main properties (homotopy, thinness and medialness). From a practical point of view, we define a benchmark for validating the quality of medial surfaces for medical applications.

Our two step method for medial surface computation is based on the ridges of the distance map. We use a medial map (called Geometric Steerable Medial Map, GSM2) based on ridge detectors that combines the advantages of steerable filters and level sets geometry [41]. In a second step, we use Non-Maxima Suppression (NMS) [9,42] to binarize GSM2 and obtain a one pixel wide medial surface. A binarization based on NMS does not depend on any topological definition and, given that regardless of the space dimension it only requires one direction to be defined, it scales well across the number of dimensions. For a reliable implementation of the methodology in clinical applications, we devote special attention to the analysis of the parametric values and their impact in the performance of the whole strategy.

Our experiments define a solid validation protocol for statistical analysis of the capability of our method to fulfill the 3 main properties that a medial surface should satisfy regardless of the medial topology and volume geome-

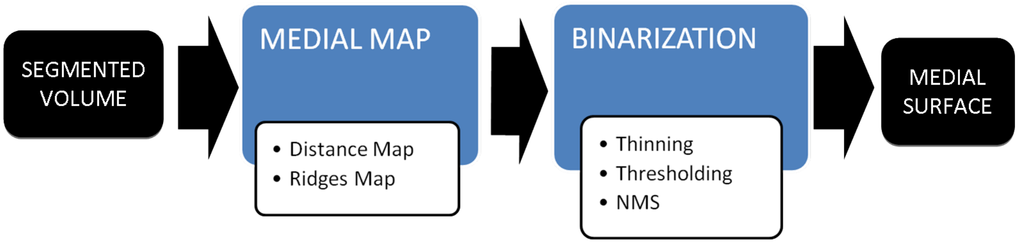

Fig. 2: Main steps in the generation of a medial surface.

try. The quality of medial structures is assessed on a benchmark of synthetic shapes of known medial geometry. The performance of our method is compared to existing topological thinning and pruning techniques. Finally, we present an application for representation of abdominal volumes that shows the reconstruction capabilities and higher ability of GSM2 to locate pathologic deformations. This experiment also illustrates the potential for pruning medial surfaces consistently with the object boundary geometry.

The contents are organized as follows. Section 2 introduces our operator for reliable computation medial structures, including details about parameter setting in Section 2.2. Section 3 presents our benchmark for validation of medial surface quality. Section 4 reports our experiments on synthetic shapes (section 4.1) and volume reconstruction of medical volumes (section 4.2). Finally, conclusions and future work are exposed in Section 5.

2 Medial Surfaces Capturing the Essential Geometry of Volumes

The computation of medial manifolds from a segmented volume may be split into two main steps (as depicted in Fig. 2): computation of a medial map from the original volume and binarization of such map. Medial maps should achieve a discriminant value on the shape central voxels. Meanwhile, the binarization step should ensure that the resulting medial structures fulfil the three conditions: medialness, thinness and homotopy.

Distance transforms are the basis for obtaining medial manifolds in any dimension. The distance map is generated by computing the Euclidean distance transform of the binary mask representing the volumetric shape. By definition, the maximum values of the distance map are located at the center of the shape at voxels corresponding to the medial structure. It follows that the medial surface could be extracted from the raw distance map by an iterative thinning process [30]. Two alternative binarizations that scale well with dimension are thresholding and NMS. Thresholding keeps pixels with medial map energy above a given value. Therefore, it requires that the medial map is constant along the medial surface. Non-Maxima Suppression keeps only these pixels attaining a local maximum of the medial map in a given direction. Unless the medial map maxima are flat, NMS also produces one pixel-wide surfaces.

Further examination of the distance map shows that its central maximal voxels are connected and constitute a ridge surface of the distance map. We propose using a normalized ridge map with NMS-based binarization for computing medial surfaces.

Ridges/valleys in a digital N-Dimensional image are defined as the set of points that are extrema (minima for ridges and maxima for valleys) in the direction of greatest magnitude of the second order directional derivative [18]. In image processing, ridge detectors are based either on level sets geometry [26] or image intensity profiles [14].

The map described in [26] defines ridges as lines joining points of maximum curvature of the distance map level sets. This operator yields homogeneous ridge responses with a high medialness discrimination power. It is computed using the maximum eigenvector of the structure tensor of the distance map as follows.

Let D denote the distance map to the shape and let its gradient, ∇D, be computed by convolution with partial derivatives of a Gaussian kernel:

$$\nabla D = (\partial_x D_\sigma, \partial_y D_\sigma, \partial_z D_\sigma) = (\partial_x g_\sigma * D, \partial_y g_\sigma * D, \partial_z g_\sigma * D)$$

being g_σ a Gaussian kernel of variance σ and ∂_x, ∂_y and ∂_z partial derivative operators. The structure tensor or second order matrix [5] is given by averaging the projection matrices onto the distance map gradient:

$$ST_{\rho,\sigma}(D) = \begin{pmatrix} g_\rho * \partial_x D_\sigma^2 & g_\rho * \partial_x D_\sigma \partial_y D_\sigma & g_\rho * \partial_x D_\sigma \partial_z D_\sigma \\ g_\rho * \partial_x D_\sigma \partial_y D_\sigma & g_\rho * \partial_y D_\sigma^2 & g_\rho * \partial_y D_\sigma \partial_z D_\sigma \\ g_\rho * \partial_x D_\sigma \partial_z D_\sigma & g_\rho * \partial_y D_\sigma \partial_z D_\sigma & g_\rho * \partial_z D_\sigma^2 \end{pmatrix} \tag{1}$$

for g_ρ a Gaussian kernel of variance ρ. Let V be the eigenvector of principal eigenvalue of $ST_{\rho,\sigma}(D)$ and consider its reorientation $\tilde{V}$ along the distance gradient, $\nabla D = (P, Q, R)$, given as:

$$\tilde{V} = \mathrm{sign}(< \mathbf{V} \cdot \nabla D >) \cdot \mathbf{V}$$

for $< \cdot >$ the scalar product. The ridgeness measure [26] is given by the divergence:

$$NRM := \mathrm{div}(\tilde{V}) = \partial_x P + \partial_y Q + \partial_z R \tag{2}$$

The above operator assigns positive values to ridge pixels and negative values to valley ones. The more positive the value is, the stronger the ridge pattern is. A main advantage over other operators (such as second order oriented Gaussian derivatives) is that NRM $\in [-N, N]$ for N the dimension of the volume. In this way, it is possible to set a threshold common to any volume for detecting significant ridges and, thus, points likely belong to the medial surface.

However, by its geometric nature, NRM has two main limitations. In order to be properly defined, NRM requires that the vector $\mathbf{V}$ uniquely defines the tangent space to image level sets. Therefore, the operator achieves strong responses in the case of one-fold medial manifolds, but significantly drops anywhere two or more medial surfaces intersect each other. Additionally, NRM responses are not continuous maps but step-wise almost binary images (see Fig.3, left). Such discrete nature of the map is prone to hinder the performance of the NMS binarization step that removes some internal voxels of the medial structure and, thus, introduces holes in the final medial surface.

On the other side, ridge maps based on image intensity are computed by convolution with a bank of steerable filters [14]. Each filter is defined by 2nd derivatives of (oriented) anisotropic 3D Gaussian kernels:

$$g_\sigma^\Theta = g_{(\sigma_x,\sigma_y,\sigma_z)}^{(\theta,\phi)} = \frac{1}{(2\pi)^{3/2}\sigma_x\sigma_y\sigma_z} e^{-\left(\frac{\tilde{x}^2}{2\sigma_x^2}+\frac{\tilde{y}^2}{2\sigma_y^2}+\frac{\tilde{z}^2}{2\sigma_z^2}\right)}$$

for $(\tilde{x},\tilde{y},\tilde{z})$ the coordinates given by rotations of angles θ and ϕ that transform the z-axis into the unitary vector $(\cos\phi\cos\theta, \cos\phi\sin\theta, \sin\phi)$. We note that by tuning the anisotropy of the Gaussian, we can detect independently medial surfaces and medial axes. For detecting sheet-like ridges, the scales should be set to $\sigma_z < \sigma_x = \sigma_y$, while for medial axes they should fulfill $\sigma_z < \sigma_x < \sigma_y$.

The second partial derivative along the z axis constitutes the principal kernel for computing ridges:

$$\partial_z^2 g_\sigma^\Theta = (\tilde{z}^2/\sigma_z^4 - 1/\sigma_z^2) g_\sigma^\Theta \tag{3}$$

The response of the operator is calculated as the maximum response for a discrete sampling of the angulation and the scale:

$$SGR := \max_{i,j,k} \left(\partial_z^2 g_{\sigma_k}^{\Theta_{i,j}} * D\right) \tag{4}$$

for $\Theta_{i,j}$ given by $\theta_i = \{i\frac{\pi}{N}, \forall i = 1,\dots,N\}$ and $\phi_j = \{j\frac{\pi}{M}, \forall j = 1,\dots,M\}$ and $\sigma_k = (\sigma_x^k, \sigma_y^k, \sigma_z^k) = (2^{k+1}, 2^{k+1}, 2^k), k = [0, K]$.

A main advantage of using steerable filters is that their response provides continuous maps which ensure completeness of the surfaces obtained by NMS binarization. Besides, since they decouple the space of possible orientations for medial surfaces, their response does not decrease at self-intersections (see Fig. 3, center). Their main counterpart is that their response is not normalized, so setting the threshold for binarization becomes a delicate issue.

The analysis above shows that geometric and intensity methods have complementary advantages and shortcomings. Therefore, we propose [42] combining them into the following Geometric Steerable Medial Map (GSM2):

$$GSM2 := SGR(NRM) \tag{5}$$

Given that the properties of medial surfaces are determined by the medial map, the advantages of GSM2 are two-fold. On one hand, steerable filters provide a continuous approximation to NRM semi-discrete maps with a more uniform response at self-intersecting points. On the other hand, because NRM maps have a sharp response at central voxels, GSM2 still provides a highly selective response at ridges. In this manner GSM2 generates medial maps with good combination of specificity in detecting medial voxels while having good characteristics for NMS binarization, which requires a continuous response in

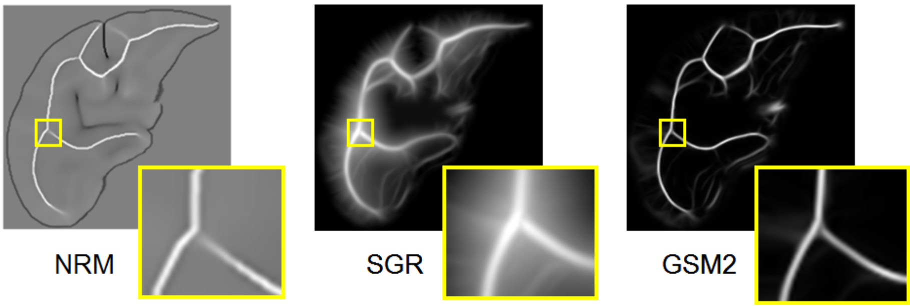

Fig. 3: Performance of different ridge operators. The geometric NRM (left) produces highly discriminant ridge values. Steerable Gaussian filters (center) are less sensible to strong ridges while having increased sensitivity to small, secondary ridges. Finally, the combined approach GSM2 (right) inherits the strong features of each approach.

order to avoid internal holes. Finally, GSM2 allows the algorithm to focus on the (shape) relevant medial structures, while small ridges, due to noise in the shape frontier can be ignored. While working with medical image segmentations this means that GSM2 allows to gather the anatomically relevant surfaces while largely ignoring small spurious manifolds.

2.1 Non-Maxima Suppression Binarization

The usage of NMS allows to obtain the voxels with higher ridgeness value and obtain a thin, one pixel wide medial surface. NMS consists in checking the two neighbors of a pixel in a specific direction, $V = (V_x, V_y, V_z)$, and delete pixels if their value is not the maximum one. Let $\mathcal{R}$ be a generic ridge map, then its NMS map along the direction V is given by:

$$NMS_{\mathcal{R}}(x,y,z) = \begin{cases} \mathcal{R}(x,y,z) & \text{if } \mathcal{R}(x,y,z) > \max(\mathcal{R}_{V+},\, \mathcal{R}_{V-}) \\ 0 & \text{otherwise} \end{cases}$$

for $\mathcal{R}_{V+} = \mathcal{R}(x+V_x, y+V_y, z+V_z)$ and $\mathcal{R}_{V-} = \mathcal{R}(x-V_x, y-V_y, z-V_z)$. A thresholding of $NMS_{\mathcal{R}}$ produces 1-pixel wide surfaces.

The search direction for local maxima is obtained from the structure tensor of the ridge map, $ST_{\rho,\sigma}(GSM2)$. Its eigenvector of greatest eigenvalue indicates the direction of highest variation of the ridge image and that direction is perpendicular to the medial surface plane. NMS image must be binarized to generate a final medial surface image. As GSM2 produces consistent values along ridges thanks to its normalized origin (NRM), the value τ suited to binarize the ridges can be obtained via basic histogram threshold calculation, such as Otsu thresholding.

2.2 Parameter Setting

Unlike most of existing parametric methods, the theoretical properties of GSM2 provide a natural way of setting parametric values regardless of the volume size and shape. Our method depends on the parameters involved in the definition of the map GSM2 and in the NMS binarization step.

The parameters arising in the definition of GSM2 are the derivation, σ, and integration, ρ, scales of the structure tensor $ST_{\rho,\sigma}(D)$ used to compute NRM and the scales, $\sigma_k = (\sigma_x^k, \sigma_y^k, \sigma_z^k)$, and orientations, $\Theta_{i,j}$, defining the steerable filter bank in (5). The derivation scale σ is used to obtain regular gradients in the case of noisy images. The larger it is the more regular the gradient will be at the cost of losing contrast. The integration scale ρ used to average the projection matrices corresponds to time in a solution to the heat equation with initial condition the projection matrix. Therefore large values provide a regular extension of the level sets normal vector, which can be used for contour closing [16]. Since in our case we apply NRM to a regular distance map with well defined completed ridges, σ and ρ can be set to their minimum values, $\sigma = 0.5$ and $\rho = 1$. Concerning steerable filters parameters, scale depends on the thickness of the ridge and orientations on the complexity of the ridge geometry. The selection of the scale might be critical in the general setting of natural scenes [23]. However in our case, SGR is applied to a normalized ridge map that defines step-wise almost binary images of ridges (see Fig. 3, left). Therefore, the choice of scale is not critical anymore. In order to get medial maps as accurate as possible, we recommend using a minimum anisotropic setting: $\sigma_z = 1$, $\sigma_x = \sigma_y = 2$. Finally, orientation sampling should be dense enough in order to capture any local geometry of medial surfaces. In the case of using the minimum scale, eight orientations, $N = M = 8$, are enough.

It follows that GSM2 is given by:

$$GSM2 = \max_{i,j} \left(\partial_z^2 g_{(2,2,1)}^{\Theta_{i,j}} * NRM \right) \tag{6}$$

for NRM computed over $ST_{1,0.5}(D)$ and $\Theta_{i,j}$ computed setting $N = M = 8$.

The parameters involved in NMS binarization step are the scales of the structure tensor $ST_{\rho,\sigma}(GSM2)$ and the binarizing threshold, τ. Like in the case of NRM, $GSM2$ is a regular function which maximums define closed medial manifolds, so we set the structure tensor scales to their minimum values $\sigma = 0.5$ and $\rho = 1$. Concerning τ, it can be obtained using any histogram threshold calculation, since $GSM2$ inherits the uniform discriminative response along ridges of NRM.

3 Validation Benchmark

In order to address the representation of organs for medical use, medial representations should achieve a good reconstruction of the full anatomy and guarantee that the boundaries of the organ are reached from the medial surface. Given that small differences in algorithm criteria can generate different surfaces, we are interested in evaluating the quality of the generated manifold as a tool to recover the original shape.

Validation in the medical imaging field is a delicate issue due to the difficulties for generating ground truth data and quantitative scores valid for reliable application to clinical practice. In this section, we propose a benchmark for evaluating medial surface quality in the context of medical applications. The benchmark is divided in two tests. The first test evaluates the quality of the medial surface generated, while the second one explores the capabilities of the generated surfaces to recover the original volume and describing anatomical structures.

3.1 Medial Surface Quality

Surface quality tests start from known medial surfaces, that will be considered as ground truth. From this surfaces, volumetric objects can be generated by placing spheres of different radii at each point of the surface. The newly created object is then used as input to several medial surface algorithms and the resulting medial surfaces, compared with the ground truth.

The test set of synthetic volumes / surfaces aims to cover different key aspects of medial surface generation (see first row in Fig.4). The first batch of surfaces (labelled 'Simple') includes objects generated with a single medial surface. A second batch of surfaces is generated using two intersecting medial surfaces (labelled 'Multiple'), while a last batch of objects (labelled 'Homotopy') covers shapes with different number of holes. Each family of medial topology has 20 samples. The volumetric object obtained from a surface can be generated by using spheres of uniform radii (identified as 'UnifDist') or with spheres of varying radii (identified as 'VarDist').

Volumes are constructed by assigning a radial coordinate to each medial point. In the case of UnifDist, all medial points have the same radial value, while for VarDist they are assigned a value in the range $[r_1, r_2]$ using a polynomial. The values of the radial coordinate must be in a range ensuring that volumes will not present self intersections. Therefore, the maximum range and procedure this radius is assigned depends on the medial topology:

- *Simple*. In this case, there are no restrictions on the radial range.
- *Multiple*. For branching medial surfaces, especial care must be taken at surface self-intersecting points. At these locations, radii have to be below the maximum value that ensures the the medial representation defines a local coordinate change [17]. This maximum value depends on the principal curvatures of the intersecting surfaces [17] and it is computed for each surface. Let X be the medial surface, Z denote the self-intersection points and $d(Z)$ the distance map to Z. The radial coordinate is assigned as follows:

$$R(X) = min(R(X), max(r_Z, d(Z)))$$

for $R(X)$ the value of the polynomial function and r_Z the maximum value allowed at self-intersections. In this manner, we obtain a smooth distribution of the radii ensuring volume integrity.
- *Homotopy.* In order to be consistent with the third main property of medial surfaces [30], volumes must preserve all holes of medial surfaces. In order to do so, the maximum radius r_2 is set to be under the minimum of all surface holes radii.

The quality of medial surfaces has been assessed by comparing them to ground truth surfaces in terms of surface distance [19]. The distance of a voxel y to a surface X is given by: $d_X(y) = \min_{x \in X} \|y - x\|$, for $\| \cdot \|$ the Euclidean norm. If we denote by X the reference surface and Y the computed one, the scores considered are:

1. *Standard Surface Distances*:

$$AvD = \frac{1}{|Y|} \sum_{y \in Y} d_X(y) \qquad MxD = \max_{y \in Y}(d_X(y))$$

2. *Symmetric Surface Distances*:

$$AvSD = \frac{1}{|X| + |Y|} \left(\sum_{x \in X} d_Y(x) + \sum_{y \in Y} d_X(y) \right)$$

$$MxSD = \max \left(\max_{x \in X}(d_Y(x)), \max_{y \in Y}(d_X(y)) \right)$$

Standard distances measure deviation from medialness, while differences between standard and symmetric distances indicate the presence of homotopy artifacts and presence of unnecessary medial segments.

For each family and method, we have computed quality scores statistical ranges as $\mu \pm \sigma$, for μ and σ the average and standard deviation computed over the 20 samples of each group of shapes. The Wilcoxon signed rank test [49] has been used to detect significant differences across performances.

3.2 Reconstruction Power for Clinical Applications

In medical imaging applications the aim is to generate the simplest medial surface that allows recovering the original volume without losing significant voxels. Volumes recovered from surfaces generated with the different methods are compared with ground truth volumes. In order to provide a real scenario for the reconstruction tests we have used 14 livers from the SLIVER07 challenge [19] as a source of anatomical volumes. Volumes are reconstructed by computing the medial representation [6] with radius given by the values of the distance map on the computed medial surfaces.

Comparisons with the original shape are based on the average and maximum symmetric surface distances (AvSD and MxSD described in section 4.1), as well as the following volumetric measures:

1. *Volume Overlap Error:*

$$VOE(A,B) = 100 \times \left(1 - 2\frac{|A \cap B|}{|A| + |B|}\right)$$

2. *Relative Volume Difference:*

$$RVD(A,B) = 100 \times \frac{|A| - |B|}{|B|}$$

3. *Dice coefficient:*

$$Dice(A,B) = \frac{2|A \cap B|}{|A| + |B|}$$

Aside from dice coefficient, lower metric values indicate better reconstruction capability.

4 Validation Experiments

Our validation protocol has been applied to the method described in Section 2. In order to compare to morphological methods, we have also applied it to an ordered thinning using a 6-connected neighborhood criterion for defining medial surfaces (labelled Th_6) described in [7], a 26-connected neighborhood surface test (labelled Th_{26}) following [30]. The consistency of surface pruning is tested on a pruned version of the 26-connected neighborhood method (labelled ThP_{26}) that does not allow degenerated medial axis segments and the scheme (labelled Tao_6) described in [20] that alternates 6-connected curve and surface thinning with more sophisticated pruning stages.

4.1 Medial Surface Quality

Figure 4 shows an example of the synthetic volumes in the first row and the computed medial surfaces in the remaining rows. Columns exemplify the different families of volumes generated: one (Simple in 1st and 2nd columns) and two (Multiple in 3rd and 4th columns) foil surfaces, as well as, surfaces with holes (Homotopy in 5th and 6th columns). For each kind of topology we show a volume generated with constant (1st, 3rd and 5th columns) and variable distance (2nd, 4th and last columns). We show medial surfaces in solid meshes and the synthetic volume in semi-transparent color. The shape of surfaces produced using morphological thinning strongly depends on the connectivity rule used. In the absence of pruning, surfaces, in addition, have either extra medial axes attached or extra surface branches in the case pruning is included as part of the thinning surface tests (Tao_6). On the contrary, GSM2 medial surfaces have a well defined shape matching the original synthetic surface.

Table 1 reports error ranges for the four methods and the different types of synthetic volumes, as well as total errors in the last column. For all methods,

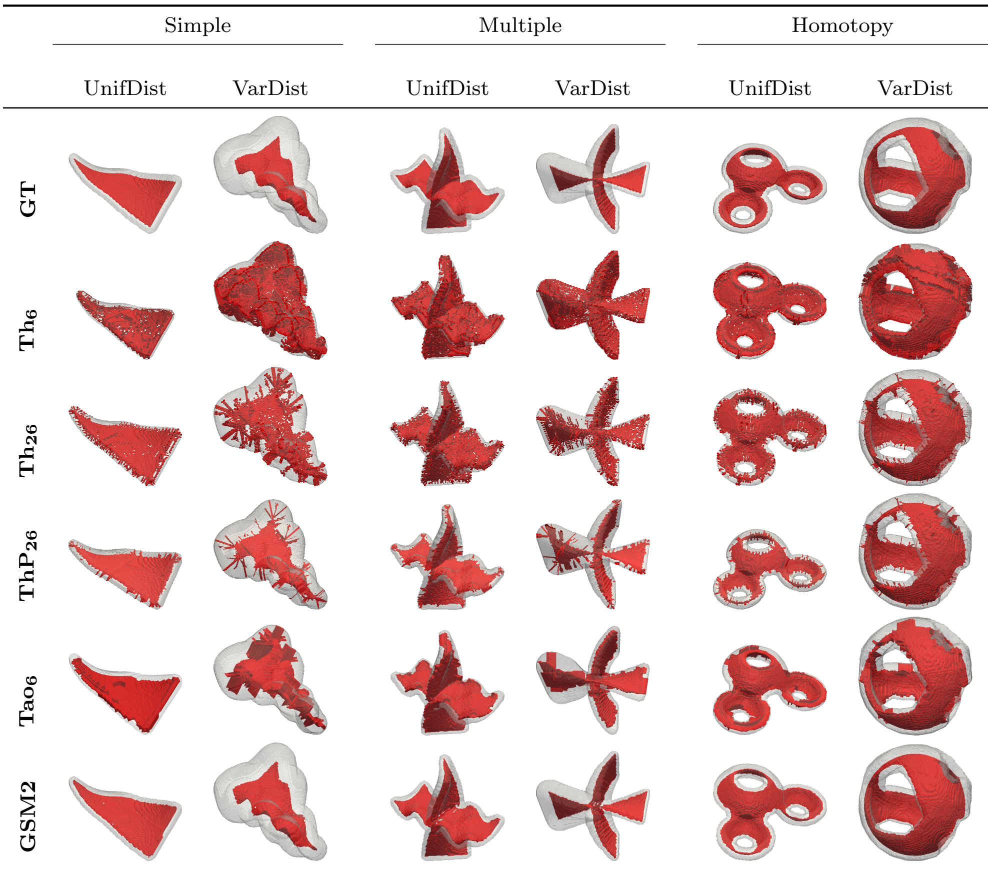

Fig. 4: Medial surfaces. Examples of the compared methods for each synthetic volume family.

there are not significant differences between standard and symmetric distances for a given volume. This indicates a good preservation of homotopy. Even with pruning, thinning has significant geometric artifacts (maximum distances increase) and might drop its performance for variable distance volumes due to a different ordering for pixel removal and type of surface preserved. According to a Wilcoxon signed rank test, strategies alternating curve and surface thinning with pruning stages have worse average distances than other morphological strategies ($p < 0.0001$ for AvD and $p < 0.0001$ for $AvSD$). Given that maximum distances do not significantly differ ($p = 0.4717$, $p = 0.6932$, $p = 0.7752$ for MxD and $p = 0.9144$, $p = 0.7463$, $p = 0.6669$ for $MxSD$), this indicates the introduction of extra structures of larger size (extra surface branches in Tao_6 for the variable volumes shown in Fig. 4).

The performance of GSM2 is significantly better than other methods (Wilcoxon signed rank test with $p < 0.0001$) presents high stability across volume geometries and produces accurate surfaces matching synthetic shapes. The small increase errors for multiple self-crossing surfaces is explained by the presence of holes at intersections between medial manifolds. Still its overall performance clearly surpasses performance of morphological approaches.

	Simple		Multiple		Homotopy		Total
	UnifDist	VarDist	UnifDist	VarDist	UnifDist	VarDist	
GSM2							
AvD	0.28 ± 0.09	0.28 ± 0.07	0.38 ± 0.09	0.43 ± 0.18	0.37 ± 0.18	0.34 ± 0.14	0.34 ± 0.14
MxD	2.99 ± 0.50	3.50 ± 1.53	3.56 ± 0.53	4.76 ± 1.51	3.39 ± 0.48	3.70 ± 0.84	3.65 ± 1.13
AvSD	0.24 ± 0.05	0.25 ± 0.05	0.37 ± 0.32	0.37 ± 0.18	0.29 ± 0.10	0.28 ± 0.08	0.30 ± 0.17
MxSD	3.02 ± 0.46	3.66 ± 1.52	4.10 ± 2.61	4.76 ± 1.51	3.39 ± 0.48	3.70 ± 0.84	3.78 ± 1.52
$\mathbf{Th_6}$							
AvD	1.52 ± 0.27	5.63 ± 2.19	1.66 ± 0.30	3.05 ± 0.75	1.56 ± 0.35	2.96 ± 1.17	2.73 ± 1.80
MxD	5.55 ± 0.26	16.21 ± 4.76	5.82 ± 0.27	10.75 ± 3.40	5.54 ± 0.20	10.17 ± 3.20	9.01 ± 4.72
AvSD	1.04 ± 0.21	4.34 ± 1.94	1.16 ± 0.24	2.24 ± 0.56	1.09 ± 0.28	2.13 ± 0.98	2.00 ± 1.48
MxSD	5.55 ± 0.26	16.21 ± 4.76	5.82 ± 0.27	10.75 ± 3.40	5.54 ± 0.20	10.17 ± 3.20	9.01 ± 4.72
$\mathbf{Th_{26}}$							
AvD	0.85 ± 0.25	3.15 ± 1.34	1.00 ± 0.19	1.89 ± 0.52	0.86 ± 0.37	1.63 ± 0.84	1.56 ± 1.07
MxD	5.51 ± 0.25	16.17 ± 4.78	5.58 ± 0.19	10.64 ± 3.43	5.46 ± 0.25	10.09 ± 3.21	8.91 ± 4.75
AvSD	0.56 ± 0.14	2.02 ± 0.92	0.67 ± 0.12	1.24 ± 0.35	0.59 ± 0.22	1.05 ± 0.56	1.02 ± 0.69
MxSD	5.51 ± 0.25	16.17 ± 4.78	5.58 ± 0.19	10.64 ± 3.43	5.46 ± 0.25	10.09 ± 3.21	8.91 ± 4.75
$\mathbf{ThP_{26}}$							
AvD	0.57 ± 0.20	2.24 ± 1.00	0.70 ± 0.17	1.38 ± 0.37	0.54 ± 0.24	1.11 ± 0.62	1.09 ± 0.79
MxD	5.49 ± 0.27	16.16 ± 4.78	5.58 ± 0.19	10.61 ± 3.43	5.41 ± 0.27	10.08 ± 3.23	8.89 ± 4.76
AvSD	0.41 ± 0.11	1.38 ± 0.61	0.50 ± 0.11	0.92 ± 0.24	0.41 ± 0.12	0.72 ± 0.37	0.72 ± 0.47
MxSD	5.49 ± 0.27	16.16 ± 4.78	5.58 ± 0.19	10.61 ± 3.43	5.41 ± 0.27	10.08 ± 3.23	8.89 ± 4.76
$\mathbf{Tao_6}$							
AvD	0.79 ± 0.21	4.82 ± 2.05	0.86 ± 0.17	2.46 ± 1.09	0.85 ± 0.29	2.48 ± 1.20	2.04 ± 1.79
MxD	4.87 ± 0.20	17.55 ± 5.19	4.92 ± 0.17	11.10 ± 3.71	4.79 ± 0.21	11.64 ± 4.33	9.14 ± 5.68
AvSD	0.51 ± 0.14	3.92 ± 1.73	0.59 ± 0.13	2.00 ± 0.96	0.59 ± 0.27	1.99 ± 1.03	1.60 ± 1.52
MxSD	4.89 ± 0.18	17.55 ± 5.19	5.32 ± 1.42	11.10 ± 3.71	5.53 ± 3.26	11.87 ± 4.25	9.38 ± 5.73

Table 1: Error ranges (mean and standard deviation) for the Synthetic Volumes

4.2 Reconstruction Power for Clinical Applications

Table 2 reports the statistical ranges for all methods and measures computed for the 14 livers. There are not significant differences among methods and best performers vary depending on the quality measure. However, our approach and the two thinnings, Th_{26P} and Tao_6, have an overall better reconstruction power.

Figure 5 shows the medial surface of healthy liver obtained with the thinning methods and Fig. 6 left, GSM2 medial surface. In the case of thinning based methods, medial manifolds have a more complex geometry than GSM2 and might include extra structures and self intersections (Fig. 5). In medical applications such extra structures might hinder the identification of abnormal or pathological structures. This is not the case for GSM2 surfaces as exemplified in Fig. 6. The oversized superior lobe on the right liver is captured by the presence of an unusual medial manifold configuration.

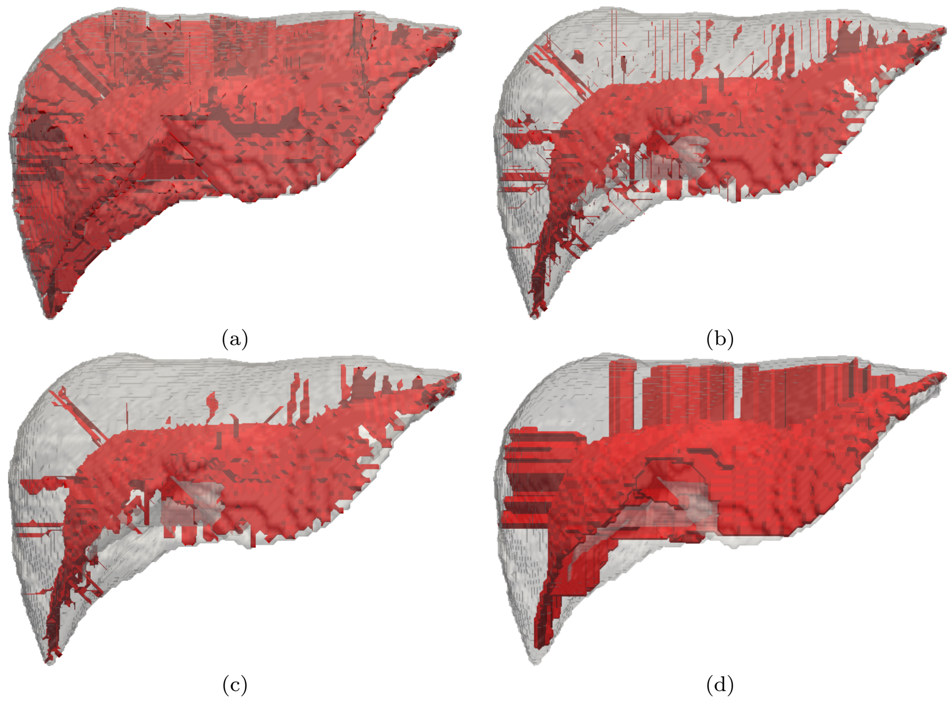

Fig. 5: Medial manifolds of a healthy liver generated with morphological methods. Th_6 (a), Th_{26} (b), ThP_{26} (c) and Tao_6 (d).

5 Conclusions and Discussion

Medial manifolds are powerful descriptors of shapes. The method presented in this paper allows the computation of medial manifolds without relying in morphological methods nor neighbourhood or surface tests. Additionally, it can be seamlessly implemented regardless of the dimension of the embedding space.

The performance of our method is compared to current morphological thinning methods in terms of the quality of medial manifolds and their capability

	$GSM2$	Th_6	Th_{26}	ThP_{26}	Tao_6
Volume Error					
VOE	7.96 ± 1.70	8.84 ± 1.73	8.25 ± 1.72	7.84 ± 1.68	8.49 ± 1.77
RVD	8.49 ± 2.03	9.10 ± 2.10	8.96 ± 2.08	7.86 ± 2.23	5.91 ± 1.99
Dice	$.959 \pm .009$	$.954 \pm .009$	$.957 \pm .009$	$.963 \pm .005$	$.955 \pm .010$
Surface Dist.					
AvSD	0.80 ± 0.06	0.89 ± 0.06	0.83 ± 0.05	0.70 ± 0.11	0.83 ± 0.06
MxSD	5.61 ± 2.68	6.00 ± 2.58	5.52 ± 2.56	5.94 ± 1.45	6.42 ± 2.33

Table 2: Mean and standard deviation of errors in volume reconstruction for each metric.

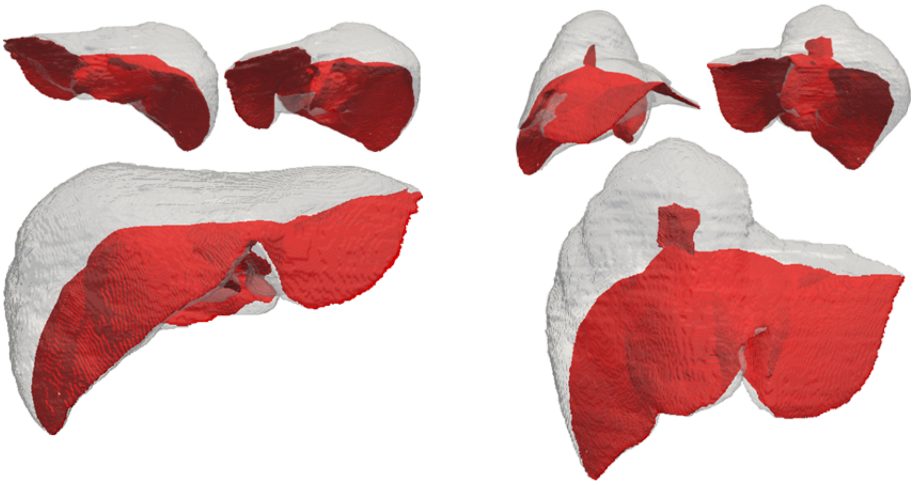

Fig. 6: Medial Manifolds of a healthy liver (left) and a liver with an unusual lobe (right).

to recover the original volume. For the first experiment a battery of synthetic shapes covering different medial topologies and volume thickness has been generated. For the second one, we have used a public database of CT volumes of livers, including pathological cases with unusual deformations. The following interesting points are derived from our experiments.

The geometry of medial manifolds obtained using morphological methods strongly depends on the description of pixel neighbourhoods. Besides, they are prone to include spurious extra branches that require a further pruning. Experiments on synthetic surfaces show that the performance depends on both medial surface topology and volume thickness. Although there are not significant differences among methods in terms of reconstruction capabilities, in medical applications extra structures hinder the identification of abnormal or pathological structures.

The proposed method has several advantages over thinning strategies. It performs equally across medial topologies and volume thickness. The resulting medial surfaces are of greater simplicity than the generated by thinning methods. Although having this minimalistic property, the resulting medial manifolds are suitable for locating unusual pathological shapes and properly restore original volumes. We conclude that our methodology reaches the best compromise between simplicity in geometry and capability for restoring the original volumetric shape.

Any simplification of a medial surface results in a drop in reconstruction quality as illustrated in the images of fig. 7. Fig. 7(a) shows a medial surface of a liver with a pruned version removing the top branch in light red. Fig. 7(b) shows the volumes reconstructed using the pruned surface (light red), as well as, the complete one (transparent black). In this case, the pruned surface cannot reconstruct the external part of the superior lobe of the liver. This drop in accuracy is hard to relate to the simplification process because the branching topology of thinning-based medial manifolds is not always related to the anatomy curvature (concavity-convexity pattern). A main advantage of GSM2 medial surfaces is that their branches are linked to the shape concavities due to the geometrical and normalized nature of the operator. In this context, GSM2 manifolds can be simplified (pruned) ensuring that the loss of reconstruction power will be minimum [43].

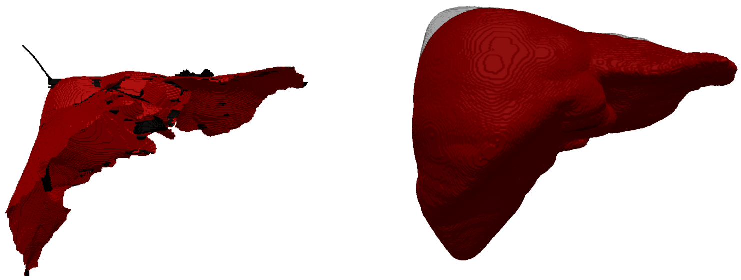

(a) (b)

Fig. 7: Impact of pruning in reconstructed volumes: medial manifolds (a) and reconstructed volumes (b).

Finally, regarding computational efficiency, our method is up to 5 times faster than thinning strategies. Unlike paralelization of topological strategies which require special treatment of topological constrains [4, 27], our code is straightforward to parallelize, even on GPU. It follows that our method could achieve the real-time speeds that clinical applications need.

The GSM2 medial map represents a clear improvement over NRM, showing improved performance at manifold intersections while retaining the normalized properties of NRM. However, the NMS step still limits the binarization to a single direction around auto-intersections. Even if the medial map achieves a uniform response at branches, binarization using NMS is likely to break branch connectivity. The NMS step keeps points achieving a local maxima along a direction that represents the normal to medial surfaces. It follows that NMS is consistent as far as surfaces have a well-defined unique normal vector that can be computed by means of the structure tensor. Branches are loci of surface self-intersections and, thus, their normal space is generated by the normal vectors of the surface intersecting folds. This singular feature influences the computation of NMS from both a theoretical and a practical point of view. On one hand, from a theoretical point of view, the definition of NMS should take into account multiple search directions at branching points. On the other hand, the primary eigenvector of the structure tensor used to compute NMS provides an average of the folds normal vectors. This average does not have to be, in practice, perpendicular to any of the intersecting fold and, thus, the ridge map is unlikely to attain a maximum in that direction. This represents a limitation at auto-intersections, which might present small holes due to a wrong direction for NMS. We are currently improving NMS binarization by adding multiple directions for local maxima search.

Future work also includes the use of the medial surfaces computed using our methods as basis for shape parametrization [52], in order to construct anatomy-based reference systems for implicit registration and localization of pathologies. Further, we will explore correspondences between medial representations of neighboring organs to define inter-organ relations in a more exhaustive way than simply using centroid and pose parameters [24, 25, 50].

Acknowledgements This work was supported by the Spanish projects TIN2009-13618, TIN2012-33116, CSD2007-00018 and the *Generalitat de Catalunya* project 2009-TEM-00007. The 2nd author has been supported by the Ramon y Cajal Program of the Spanish Ministry of Economy and Competitiveness.

References

1. Ahuja, N., Chuang, J.H.: Shape representation using a generalized potential field model. Pattern Analysis and Machine Intelligence, IEEE Transactions on **19**(2), 169 –176 (1997)
2. Amenta, N., Bern, M.: Surface reconstruction by voronoi filtering. Discrete and Computational Geometry **22**, 481–504 (1998)
3. Amenta, N., Choi, S., Kolluri, R.: The power crust, unions of balls, and the medial axis transform. Computational Geometry: Theory and Applications **19(2-3)**, 127–153 (2001)
4. B., G.: A parallel thinning algorithm for medial surfaces. Pattern Recognition Letters **16(9)**, 979–986 (1995)
5. Bigun, J., Granlund, G.: Optimal orientation detection of linear symmetry. In: ICCV, pp. 433–438 (1987)
6. Blum, H.: A transformation for extracting descriptors of shape. MIT Press (1967)
7. Bouix, S., Siddiqi, K.: Divergence-based medial surfaces. In: ECCV, pp. 603–618 (2000)
8. Bouix, S., Siddiqi, K., Tannenbaum, A.: Flux driven automatic centerline extraction. Med. Imag. Ana. **9**(3), 209–21 (2005)
9. Canny, J.: A computational approach to edge detection. IEEE Trans. Pat. Ana. Mach. Intel. **8**, 679–698 (1986)
10. Chang, M., Leymarie, F., Kimia, B.: 3d shape registration using regularized medial scaffolds. In: Proceedings of the 3D Data Processing, Visualization, and Transmission (3DPVT), pp. 987–994. IEEE Computer Society, Washington, DC, USA (2004)

11. Crouch, J., Pizer, S., Chaney, E., Hu, Y.C., Mageras, G., Zaider, M.: Automated Finite-Element analysis for deformable registration of prostate images. Medical Imaging, IEEE Transactions on **26**(10), 1379–1390 (2007)
12. Dey, T.K., Zhao, W.: Approximate medial axis as a voronoi subcomplex. In: Proceedings of the seventh ACM symposium on Solid modeling and applications, SMA '02, pp. 356–366. ACM (2002)
13. Fletcher, P.T., Lu, C., et al.: Principal Geodesic Analysis for the study of nonlinear statistics of shape. IEEE Trans. Med. Imag. **23(8)**, 995–1005 (2004)
14. Freeman, W., Adelson, E., of Technology. Media Laboratory. Vision, M.I., Group, M.: The design and use of steerable filters. IEEE Transactions on Pattern analysis and machine intelligence **13**(9), 891–906 (1991)
15. Garcia-Barnes, J., Gil, D., A. Hernandez, A.: 3d shape registration using regularized medial scaffolds. In: Proceedings of the 3D Data Processing, Visualization, and Transmission (3DPVT), pp. 987–994. IEEE Computer Society (2004)
16. Gil, D., Radeva, P.: Extending anisotropic operators to recover smooth shapes. Comput. Vis. Image Underst. **99**(1), 110–125 (2005)
17. Gray, A.: Tubes. Birkhäuser (2004)
18. Haralick, R.: Ridges and valleys on digital images. Comput. Vision Graph. Image Process. **22(10)**, 28–38 (1983)
19. Heimann, T., van Ginneken, B., Styner, M.A., Arzhaeva, Y., Aurich, V.: Comparison and evaluation of methods for liver segmentation from CT datasets. IEEE Trans. Med. Imag. **28(8)**, 1251–1265 (2009)
20. Ju, T., Baker, M.L., Chiu, W.: Computing a family of skeletons of volumetric models for shape description. In: In Geometric Modeling and Processing, pp. 235–247 (2007)
21. Keim, D., Panse, C., North, S.: Medial-axis-based cartograms. IEEE Comput. Graph. Appl. **25**, 60–68 (2005)
22. Lee, T.C., Kashyap, R.L., Chu, C.N.: Building skeleton models via 3-D medial surface axis thinning algorithms. Grap. Mod. Imag. Process. **56**(6), 462–478 (1994)
23. Lindeberg, T.: Feature detection with automatic scale selection. International Journal of Computer Vision **30**(2), 79–116 (1998)
24. Linguraru, L., Pura, J., Chowdhury, A., Summers, R.: Multi-organ segmentation from multi-phase abdominal CT via 4D graphs using enhancement, shape and location optimization. In: Med Image Comput Comput Assist Interv., *LNCS*, vol. 13(Pt 3), pp. 89–96. Springer (2010)
25. Liu, X., Linguraru, M., Yao, J., Summers, R.: Organ pose distribution model and an MAP framework for automated abdominal multi-organ localization. pp. 393–402. Springer (2010)
26. Lopez, A., Lumbreras, F., Serrat, J., Villanueva, J.: Evaluation of methods for ridge and valley detection. IEEE Trans. Pat. Ana. Mach. Intel. **21**(4), 327–335 (1999)
27. Palagyi, K., Kuba, A.: A parallel 3d 12-subiteration thinning algorithm. Graphical Models and Image Processing **61(4)**, 199–221 (1999)
28. Pizer, S., Fletcher, P., et al.: Deformable M-Reps for 3D medical image segmentation. Int. J. Comp. Vis. **55**(2), 85–106 (2003)
29. Pizer, S., Fletcher, P., et al: A method and software for segmentation of anatomic object ensembles by deformable M-Reps. Medical Physics **32**(5), 1335–1345 (2005)
30. Pudney, C.: Distance-ordered homotopic thinning: A skeletonization algorithm for 3D digital images. Comp. Vis. Imag. Underst. **72(2)**, 404–13 (1998)
31. Sheehy, D., Armstrong, C., Robinson, D.: Shape description by medial surface construction. IEEE Trans. on Visualization and Computer Graphics **2**(1), 62–72 (1996)
32. Siddiqi, K., Bouix, S., Tannenbaum, A., Zucker, S.: Hamilton-Jacobi skeletons. Int. J. Comp. Vis. **48**(3), 215–231 (2002)
33. Stough, J., Broadhurst, R., Pizer, S., Chaney, E.: Regional appearance in deformable model segmentation **4584**, 532–543 (2007)
34. Styner, M., Gerig, G., Lieberman, J., Jones, D., Weinberger, D.: Statistical shape analysis of neuroanatomical structures based on medial models (3), 207–220 (2003)
35. Styner, M., Lieberman, J.A., D., P., Gerig, G.: Boundary and medial shape analysis of the hippocampus in schizophrenia. Medical Image Analysis **8**(3), 197–203 (2004)

36. Sun, H., Avants, B., Frangi, A., Sukno, F., Gee, J., Yushkevich, P.: Cardiac medial modeling and time-course heart wall thickness analysis. In: MICCAI, vol. 5242, pp. 766–773 (2008)
37. Sun, H., Frangi, A.F., Wang, H., et al: Automatic cardiac mri segmentation using a biventricular deformable medial model. In: MICCAI, vol. 6361, pp. 468–475. Springer (2010)
38. Svensson, S., Nyström, I., di Baja, G.S.: Curve skeletonization of surface-like objects in 3d images guided by voxel classification. Pattern Recognition Letters **23(12)**, 1419–1426 (2002)
39. Terriberry, T., Gerig, G.: A continuous 3-d medial shape model with branching. In: International Workshop on Mathematical Foundations of Computational Anatomy MFCA-2006, in conjunction with MICCAI (2006)
40. Udrea, R.M., Vizireanu, N.: Iterative generalization of morphological skeleton. Journal of Electronic Imaging **16**(1), 010,501–010,501–3 (2007)
41. Vera, S., Gil, D., Borràs, A., Sánchez, X., Pérez, F., Linguraru, M.G., Ballester, M.A.G.: Computation and evaluation of medial surfaces for shape representation of abdominal organs. In: LNCS. Springer (2010)
42. Vera, S., Gonzalez, M.A., Gil, D.: A medial map capturing the essential geometry of organs. In: Proceedings of ISBI. IEEE (2012)
43. Vera, S., González, M.A., Linguraru, M.G., Gil, D.: Optimal medial surface generation for anatomical volume representations. In: Abdominal Imaging. Computational and Clinical Applications, *Lecture Notes in Computer Science*, vol. 7601, pp. 265–273 (2012)
44. Vizireanu, D.N.: Generalizations of binary morphological shape decomposition. J. Electronic Imaging **16**(1), 013,002 (2007)
45. Vizireanu, D.N.: Morphological shape decomposition interframe interpolation method. Journal of Electronic Imaging **17**(1), 013,007–013,007–5 (2008)
46. Vizireanu, N., Halunga, S., Marghescu, G.: Morphological skeleton decomposition interframe interpolation method. Journal of Electronic Imaging **19**(2), 023,018–023,018–3 (2010)
47. Vizireanu, N., Udrea, R.M.: Visual-oriented morphological foreground content grayscale frames interpolation method. J. Electronic Imaging **18**(2), 020,502 (2009)
48. Wade, L., Parent, R.: Automated generation of control skeletons for use in animation. The Visual Computer **18**, 97–110 (2002)
49. Wilcoxon, F.: Individual comparisons by ranking methods. Biometrics Bulletin **1(6)**, 80–83 (1945)
50. Yao, J., Summers, R.: Statistical location model for abdominal organ localization. In: MICCAI, *LNCS*, vol. 12(Pt 2), pp. 9–17. Springer (2009)
51. Yushkevich, P.: Continuous medial representation of brain structures using the biharmonic PDE. NeuroImage **45**(1), 99–110 (2009)
52. Yushkevich, P., Zhang, H., Gee, J.: Continuous medial representation for anatomical structures. IEEE Trans. Medical Imaging **25**(12), 1547–64 (2006)
53. Yushkevich, P., Zhang, H., Simon, T., Gee, J.: Structure-specific statistical mapping of white matter tracts. NeuroImage **41**(2), 448–461 (2008)